Anomalous dynamical response of non-Hermitian topological phases

Ritu Nehra [1,2,*] and Dibyendu Roy [1,†]
[1]*Raman Research Institute, Bangalore-560080, India*
[2]*Department of Physics, Ben-Gurion University of the Negev, Beer-Sheva 84105, Israel*

(Received 6 November 2023; revised 7 March 2024; accepted 14 March 2024; published 27 March 2024)

Composite topological phases with intriguing topology like Möbius strips emerge in sublattice symmetric non-Hermitian systems due to spontaneous breaking of time-reversal symmetry at some parameter regime. While these phases have been characterized by nonadiabatic complex geometric phases of multiple participating complex bands, the physical properties of these phases remain largely unknown. We explore the dynamical response of these phases by studying Loschmidt echo from an initial state of the Hermitian Su-Schrieffer-Heeger (SSH) model, which is evolved by a non-Hermitian SSH Hamiltonian after a sudden quench in parameters. Topology-changing quenches display nonanalytical temporal behavior of return rates (logarithm of the Loschmidt echo) for the non-Hermitian SSH Hamiltonian in the trivial, Möbius, and topological phase. Moreover, the dynamical topological order parameter appears only at one side of the Brillouin zone for the Möbius phase case in contrast to both sides of the Brillouin zone for quench by the trivial and topological phase of the non-Hermitian SSH model. The last feature is a dynamical signature of different symmetry constraints on the real and imaginary parts of the complex bands in the Möbius phase.

DOI: 10.1103/PhysRevB.109.094311

I. INTRODUCTION

Topology and quantum dynamics are shown to be intrinsically related in the early research on topology in condensed-matter physics [1]. Several near-equilibrium dynamical quantities such as linear electrical transport [2,3], change in electrical polarization [4], and Josephson current [5] are directly connected to the underlying topology of the band structures. Recent studies have further extended the realm of their connections to the out-of-equilibrium regime. It has been found that topology-changing quenches are always followed by nonanalytic temporal behavior of return rates (logarithm of the Loschmidt echo), characterizing dynamical phase transitions (DPTs) [6–8]. Topological edge modes can further influence features of nonequilibrium transport in open topological systems [9,10]. The effective Hamiltonian of an open quantum system is non-Hermitian. In recent years, there has been massive research interest in exploring topological features in non-Hermitian models [11–20].

The energies are complex-valued in non-Hermitian systems in contrast to the Hermitian systems with real eigenvalues [21–25]. The degeneracy in the complex energy spectrum and the coalescence of related eigenvectors lead to the nonanalyticities (singularities) coined exceptional points (EPs) [18,26,27]. The complex energy spectrum and the EPs pave the way for the ramification and unification of various crucial symmetries in non-Hermitian systems [28–30]. Such unification and branching out of symmetries have led to intriguing topological phases, both with and without their Hermitian counterparts. For instance, the trivial and topological phases with a complex-energy gap in a sublattice symmetric non-Hermitian Su-Schrieffer-Heeger (NSSH) model [31–37] are similar to those phases with a real-energy gap in the related Hermitian model. The NSSH model also hosts a gapless composite topological phase named the Möbius phase in the parameter region between two EPs. The Möbius phase involves the multiple participating complex bands [11,12,30] and does not have a Hermitian analog.

Our main aim of this study is to identify physical signatures of these non-Hermitian phases, particularly the gapless Möbius phase. We are not aware of any study exploring equilibrium or out-of-equilibrium physical properties of the Möbius phase yet. We explore here the global dynamical features arising from the integration or disintegration of different crucial symmetries and the accompanying topological phases of the NSSH model. We study the Loschmidt echo from an initial state of the Hermitian SSH model, which is evolved by an NSSH Hamiltonian after a sudden quench in parameters [38]. Previous studies on the Loschmidt echo with non-Hermitian topological models have mostly considered parity-time ($\mathcal{PT}$) symmetric models [39–41], apart from a few exceptions [42,43]. Nevertheless, pertinent questions remain unanswered, particularly for sublattice symmetric models, as shown here. We first show that a quench by the NSSH Hamiltonian in the Möbius phase exhibits DPTs from both the trivial and topological phase. The last feature is sharply different from the quench by a $\mathcal{PT}$ symmetric SSH Hamiltonian in the broken phase [39–41] from both phases when there is no DPT. Further, we also observe unique dynamical signatures related to the symmetry constraints in the composite phase of the sublattice symmetric NSSH model. We demonstrate these unique features in the return rates and the dynamical

*ritu@post.bgu.ac.il
†droy@rri.res.in

Cases	T ⇒ M	T ⇒ TP
Quench variables &DTOPs	$\delta_i = -0.9, \theta_i = 0$ $\delta_f = -0.1, \theta_f = 0.4$ $\nu^{BZ} = 1$	$\delta_i = -0.9, \theta_i = 0$ $\delta_f = 0.9, \theta_f = 0.4$ $\nu^{BZ} = 2$
$\phi^G(k,t)$	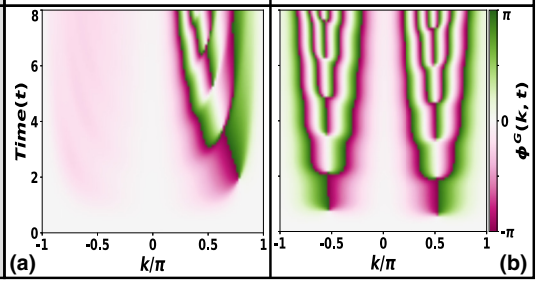	

FIG. 1. Summary of main results for two quench protocols from a trivial (T) phase of the Hermitian SSH model to a Möbius (M) and a topological (TP) phase of the non-Hermitian SSH model. The Pancharatnam phase $\phi^G(k,t)$ is calculated for a single particle with momentum k at time t. Parameters of the initial and final Hamiltonian are denoted by δ_i, θ_i and δ_f, θ_f, respectively. The number of DTOPs per Brillouin zone is represented by ν^{BZ}, which shows different ν^{BZ} for the final Hamiltonian in the M and TP phases.

topological order parameter (DTOP). We observe here two DTOPs in the Brillouin zone (BZ) for a topology-changing quench by the NSSH model in either the trivial or topological phase, and the initial state in any band. However, there is only one DTOP in the positive or negative half of the BZ when the NSSH model is in the Möbius phase. Analyzing the consequences of symmetries on the complex energy spectrum, we explain the differences in the number of the DTOPs for quench by NSSH in the topological or trivial phase versus the Möbius phase. Figure 1 summarizes our main findings.

The rest of the paper is divided into three sections. In Sec. II, we introduce the NSSH model, its complex Bloch vector and spectrum, important symmetries, and their consequences on various topological phases. We also briefly describe the non-Hermitian analogs of various dynamical quantities such as the Loschmidt echo, return rate, and DTOPs, which we apply to analyze DPTs in different quench settings. We give our main results from the various quench protocols in Sec. III and explain these results there. We conclude the paper with a summary of our main findings and some outlook for possible issues and future extensions of this research in Sec. IV. Additionally, we include Appendix to examine the impact of boundaries on dynamical quantities such as the return rate and edge occupation.

II. MODEL AND QUENCH DYNAMICS

A. Non-Hermitian SSH model

The Hamiltonian of the bipartite sublattice symmetric NSSH chain [11,12,35–37] reads

$$H = \sum_{m=1}^{L}(v_\ell a_m^\dagger b_m + v_r b_m^\dagger a_m) + \sum_{m=1}^{L-1}(w_\ell b_m^\dagger a_{m+1} + w_r a_{m+1}^\dagger b_m) + \eta(w_\ell b_L^\dagger a_1 + w_r a_1^\dagger b_L), \quad (1)$$

where $c_m^\dagger$ (c_m) represents the spinless fermionic creation (annihilation) operator at the $c = a, b$ sublattice site of the mth unit cell, and L is the length of the chain. The parameter η regulates the connection at the boundaries, and the periodic boundary condition (PBC) is obtained with $\eta = 1$. Here, v_λ (w_λ) represents the intracell (intercell) hopping amplitude with a subscript $\lambda = \ell, r$ indicating the left and right direction of hopping, respectively. The PBC allows us to write H as a 2×2 matrix in the momentum k space as

$$\mathcal{H}(k) = \begin{bmatrix} 0 & (v_\ell + w_r e^{ik}) \\ (v_r + w_\ell e^{-ik}) & 0 \end{bmatrix}. \quad (2)$$

In the rest of the paper, we parametrize as $v_\ell = v_r = J(1-\delta)$, $w_r = w_\ell e^{-\theta} = J(1+\delta)$, $\theta > 0$, which facilitate symmetric quenches and a single control of non-Hermiticity (θ). The boundaries of various topological phases can be controlled by tuning the system parameters, e.g., δ, θ. The trivial, Möbius, and topological phases appear, respectively, for $\frac{1-e^\theta}{1+e^\theta} > \delta$, $\frac{1-e^\theta}{1+e^\theta} < \delta < 0$, and $\delta > 0$ [11,12].

We can further present $\mathcal{H}(k)$ in terms of the Pauli matrices, $\vec{\sigma} = (\sigma_x, \sigma_y, \sigma_z)$, as $\mathcal{H}(k) = \vec{d}_k \cdot \vec{\sigma}$, where $\vec{d}_k = (d_k^x, d_k^y, d_k^z) \in C^3$ is a complex-valued three-dimensional Bloch vector with components as

$$d_k^x = J(1-\delta) + J(1+\delta)e^{\frac{\theta}{2}} \cos\left(k + i\frac{\theta}{2}\right),$$
$$d_k^y = -J(1+\delta)e^{\frac{\theta}{2}} \sin\left(k + i\frac{\theta}{2}\right), \; d_k^z = 0. \quad (3)$$

In the Hermitian limit ($\theta = 0$), $\vec{d}_k$ becomes the real-valued Bloch vector ($d_k^{x,y,z} \in R$) of the SSH model [44,45], whose end point traces out a closed loop on the d_k^x, d_k^y plane either encircling or excluding the origin as k is swept across the BZ, $k = -\pi \to \pi$. The bulk winding number indicating the topology of the model counts the number of times the loop winds around the origin. In Figs. 2(g)–2(i), we show the analogous plots for the real and imaginary parts of $\vec{d}_k$ of the NSSH model for three different values of δ ($= -0.9, -0.1, 0.9$). The loop by the imaginary part of $\vec{d}_k$ always includes the origin of the d_k^x, d_k^y plane. However, the loop by the real part of $\vec{d}_k$ shows interesting features in three different phases of the NSSH model. In the topological phase, it winds around both the origin and the loop by the imaginary part without intersecting the loop in Fig. 2(i). The loop by the real part of $\vec{d}_k$ avoids the origin as well as the loop by the imaginary part of $\vec{d}_k$ in the trivial phase as shown in Fig. 2(g). For the Möbius phase, the loops by the real and imaginary parts of $\vec{d}_k$ intersect, and the loop by the real part may or may not include the origin as in Fig. 2(h). Comparing the Bloch vector between the Hermitian and non-Hermitian case in Eq. (3), we find a modification of the intercell hopping as $J(1+\delta)e^{\frac{\theta}{2}}$, and an emergence of complex-valued momentum $k' = k + i\frac{\theta}{2}$ in the non-Hermitian model, which lead to various kinds of skin effects [46–49] in such a model.

The complex energy eigenvalues of the two bands of the NSSH model are

$$E_\pm(k) = \pm\epsilon_k = \pm\sqrt{(v_\ell + w_r e^{ik})(v_r + w_\ell e^{-ik})}. \quad (4)$$

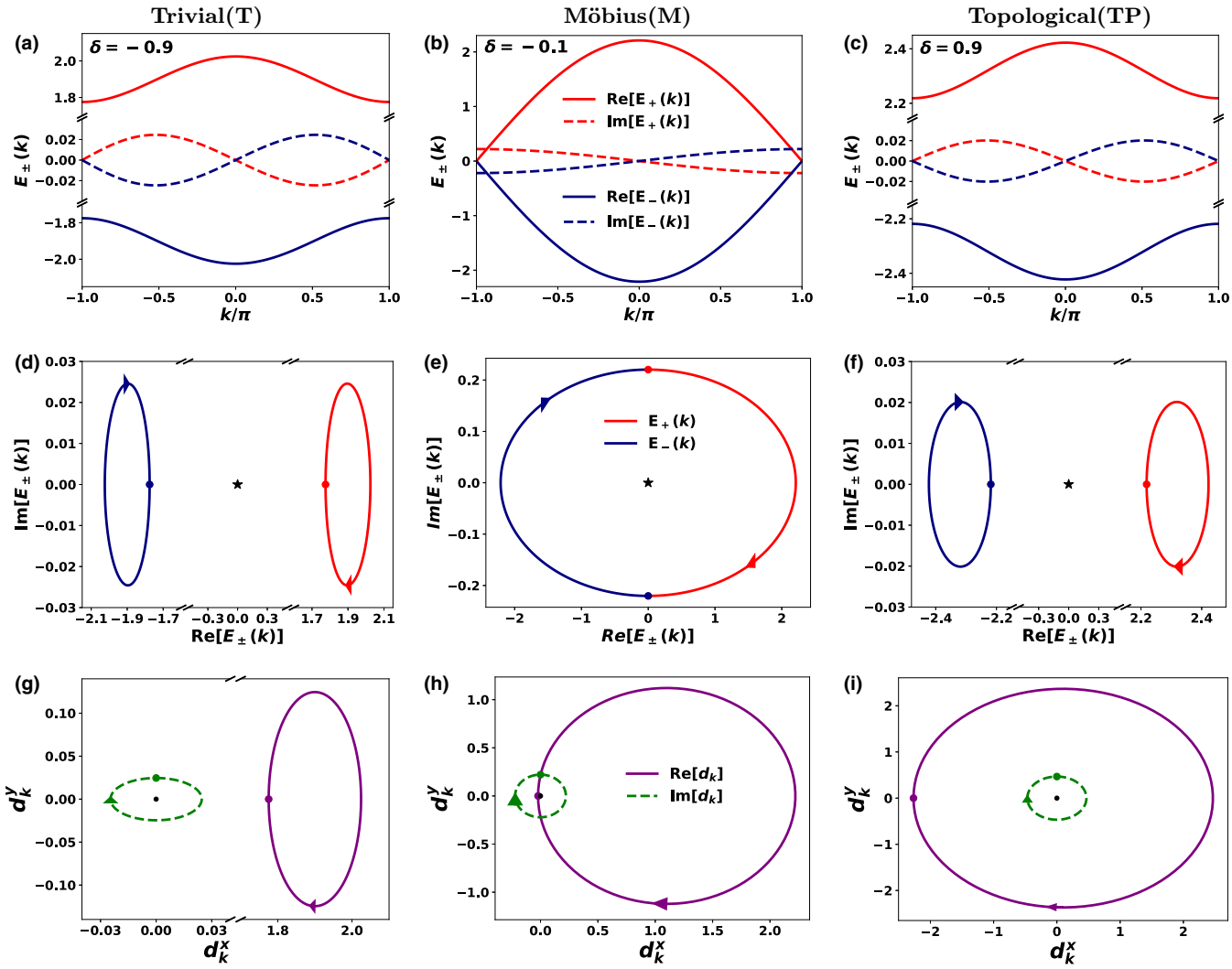

FIG. 2. The complex energy spectrum $E_\pm(k)$ with momentum k (top row) and on the parametric space of $\mathrm{Re}[E_\pm(k)]$ and $\mathrm{Im}[E_\pm(k)]$ (middle row) in three different phases of the non-Hermitian SSH model. The contour of the end points of the real (full line) and imaginary (dashed line) parts of $\vec{d}_k$ is shown on the d_k^x, d_k^y plane as k is swept across the Brillouin zone, $k = -\pi \to \pi$ (bottom row). The parameters are $J = 1$, $\theta = 0.4$, and $\delta = -0.9$ (trivial), -0.1 (Möbius), and 0.9 (topological). The dot represents a value at $k = -\pi$ and the arrow indicates $k = -\pi \to \pi$ for complex energy $E_\pm(k)$ and Bloch vector $\vec{d}_k$ in the middle and bottom rows. The exceptional point and the origin of the d_k^x, d_k^y plane are shown by a black star and a dot, respectively.

We show the real (full lines) and imaginary (dashed lines) parts of $E_p(k)$ for $p = \pm$ with k in Figs. 2(a)–2(c) for three different values of δ $(= -0.9, -0.1, 0.9)$ representing the trivial, Möbius, and topological phases of the non-Hermitian chain. The biorthogonal eigenvectors to the corresponding eigenvalues $\pm\epsilon_k$ are

$$|\psi_k^\pm\rangle = \frac{1}{\sqrt{2}}\Big(\frac{v_\ell + w_r e^{ik}}{\epsilon_k}\tilde{a}_k^\dagger \pm \tilde{b}_k^\dagger\Big)|0\rangle, \tag{5}$$

$$\langle\chi_k^\pm| = \langle 0|\frac{1}{\sqrt{2}}\Big(\frac{v_r + w_\ell e^{-ik}}{\epsilon_k}\tilde{a}_k \pm \tilde{b}_k\Big), \tag{6}$$

where $\tilde{c}_k^\dagger$ $(\tilde{c}_k)$ is the fermionic creation (annihilation) operator at the $c = a, b$ sublattice with a momentum k.

The NSSH chain with nonreciprocal hoppings has antiunitary symmetries, time-reversal symmetry (TRS) $\mathcal{T}K$ and particle-hole symmetry (PHS†) $\mathcal{C}K$, and unitary sublattice symmetry (SLS) $\mathcal{S}$ given by the following relations: $\mathcal{T}^{-1}\mathcal{H}^*(k)\mathcal{T} = \mathcal{H}(-k)$, $\mathcal{C}^{-1}\mathcal{H}^*(k)\mathcal{C} = -\mathcal{H}(-k)$, and $\mathcal{S}^{-1}\mathcal{H}(k)\mathcal{S} = -\mathcal{H}(k)$, where $\mathcal{T} = \sigma_0, \mathcal{C} = \sigma_z, \mathcal{S} = \sigma_z$, with σ_0 being a 2×2 identity matrix and K is the complex-conjugate operator [50]. The complex energy bands individually respect the TRS in all three phases: $E_\pm(k) = E_\pm^*(-k)$. The SLS indicates that the bands appear as opposite-sign pairs. The TRS gives $\mathrm{Re}[E_\pm(k)] = \mathrm{Re}[E_\pm(-k)]$ and $\mathrm{Im}[E_\pm(k)] = -\mathrm{Im}[E_\pm(-k)]$, which indicate that the real and imaginary parts of the complex bands are, respectively, an even and odd function of k. The SLS indicates that the real or imaginary part of the two complex bands is of the same magnitude and an opposite sign at any k. Nevertheless, the bands do not respect individually PHS† in any phase. Rather, the complex bands are paired via PHS†: $E_\pm(k) = -E_\mp^*(-k)$. The TRS and PHS† make the complex spectrum symmetric about the real and imaginary axis, respectively, as we show

in Figs. 2(d)–2(f). These plots also display a complex-energy gap in the trivial and topological phases, and no gap in the Möbius phase.

When a state is a simultaneous eigenstate of the Hamiltonian and TRS or SLS, the energy of the state is either purely real or zero. The states at time-reversal-invariant momenta $k = 0, \pm\pi$ in the topological and trivial phase for PBC, and the edge states for open or special boundary conditions [11,12] in the topological phase, follow the above constraints on energy. However, such consequences of the TRS and SLS break down in the Möbius phase for $\delta \in (\frac{1-e^{\theta}}{1+e^{\theta}}, 0)$ at $k = \pm\pi$ for PBC as well as for the special boundary condition, when two purely imaginary energy modes emerge. The appearance of purely imaginary energy modes can be associated with the emergence of the simultaneous eigenstate of the Hamiltonian and PHS† in the intriguing Möbius phase in the parameter region between two EPs [11,12]. Recent works [11,12,51,52] point out the application of different adiabatic and nonadiabatic topological invariants for characterizing these nontrivial topological phases with and without Hermitian counterparts. We explore here the dynamical features of these non-Hermitian topological phases with the help of the Loschmidt echo and DTOP.

B. Loschmidt echo

The Loschmidt echo [53,54] measures the extent to which a quantum evolution can reverse upon an imperfect time reversal. It is achieved by employing slightly different forward and backward time-evolving Hamiltonians. The Loschmidt echo in Hermitian setups has been explored quite a lot theoretically [6,8,55] as well as experimentally [56,57]. The Loschmidt echo [53,58,59] is defined as $\mathcal{L}(t) = \langle\tilde{\Psi}|e^{iH_{\rm f}t}e^{-iH_{\rm i}t}|\Psi\rangle$, where $H_{\rm i}$ and $H_{\rm f}$ are initial and final Hamiltonians with a slight difference between them. Here, $\{|\Psi\rangle, \langle\tilde{\Psi}|\}$ are mutually associated biorthogonal initial states. We choose $|\Psi\rangle$ as an eigenstate of $H_{\rm i}$, and we drop the trivial phase factor from $\mathcal{L}(t)$ due to time evolution by $H_{\rm i}$. Thus, we simplify the above definition of the Loschmidt echo [60,61] as

$$\mathcal{L}(t) = \langle\tilde{\Psi}|e^{iH_{\rm f}t}|\Psi\rangle. \tag{7}$$

In particular, $|\Psi\rangle$ is prepared as a half-filled many-body eigenstate of $H_{\rm i}$. To perform the quench study, we change $\delta_{\rm i}, \theta_{\rm i}$ characterizing $H_{\rm i}$ to $\delta_{\rm f}, \theta_{\rm f}$ for $H_{\rm f}$ at $t = 0$. We also keep $J = 1$ everywhere. An analytical description of generic quench dynamics for our model is provided below. The numerical results of the quench dynamics and Fisher zeros (FZs) are presented in the next section.

For a generic non-Hermitian $H_{\rm i}$, $|\Psi\rangle$ as a half-filled many-body eigenstate of $H_{\rm i}$ occupying the lower band reads

$$|\Psi\rangle = \prod_k |\psi_k^{\rm i,-}\rangle = \prod_k \frac{1}{\sqrt{2}}\Big(\frac{v_\ell + w_r e^{ik}}{\epsilon_k}\tilde{a}_k^{\dagger} - \tilde{b}_k^{\dagger}\Big)|0\rangle. \tag{8}$$

Using $|\Psi\rangle$ in Eq. (7), we then derive

$$\mathcal{L}(t) = \prod_k \mathcal{G}_k(t) = \prod_k \langle\chi_k^{\rm i,-}(0)|\psi_k^{\rm i,-}(t)\rangle, \tag{9}$$

where

$$\mathcal{G}_k(t) = \frac{\beta_k^{+}e^{i\epsilon_k^{\rm f}t} + \beta_k^{-}e^{-i\epsilon_k^{\rm f}t}}{N(k,t)} = \frac{\cos(\epsilon_k^{\rm f}t) - i\,\hat{d}_k^{\rm i}.\hat{d}_k^{\rm f}\sin\left(\epsilon_k^{\rm f}t\right)}{N(k,t)}, \tag{10}$$

with $\beta_k^{\mu} \equiv \langle\chi_k^{\rm i,-}|\psi_k^{\rm f,\mu}\rangle\langle\chi_k^{\rm f,\mu}|\psi_k^{\rm i,-}\rangle = (1 - \mu\,\hat{d}_k^{\rm i}\cdot\hat{d}_k^{\rm f})/2$ for $\mu = \pm$, and $\hat{d}_k^{\rm i/f} = \frac{\vec{d}_k^{\rm i/f}}{\sqrt{\vec{d}_k^{\rm i/f}\cdot\vec{d}_k^{\rm i/f}}}$. Note that the normalization of $\mathcal{L}(t)$ or $|\psi_k^{\rm i,-}(t)\rangle$ is introduced through $N(k,t) = \sqrt{\langle\chi_k^{\rm i,-}(0)|e^{-iH_{\rm f}^{\dagger}t}e^{iH_{\rm f}t}|\psi_k^{\rm i,-}(0)\rangle}$ to compensate the nonunitary time evolution by a non-Hermitian Hamiltonian. Here we use i,f either in the subscript or in the superscript of different variables to associate them with the initial and final Hamiltonian, respectively.

The return rate $[I(t)]$ characterizes how often the evolved state after the quench comes close to the initial state. It is defined as $I(t) = -\log|\mathcal{L}(t)|/L$, which in the thermodynamic limit ($L \to \infty$) reads

$$I(t) = -\frac{1}{2\pi}\oint_k \log|\mathcal{G}_k(t)|dk. \tag{11}$$

If we compare $\mathcal{L}(t)$ to the dynamical partition function for boundary state $|\Psi\rangle$ separated by $z = it$, $I(t)$ denotes the dynamical free energy for the process. The return of the evolving state $|\psi_k^{\rm i,-}(t)\rangle$ after a quench to the initial state $|\psi_k^{\rm i,-}(0)\rangle$ is characterized by $\mathcal{L}(t) = 1$ or $I(t) = 0$. The nonanalyticities in $I(t)$ indicate the DPT in the model, which occurs for $|\mathcal{L}(t)| = 0$ or $\mathcal{G}_k(t) = 0$ for any k [55]. The solutions for $|\mathcal{L}(t)| = 0$ are also known as the FZs. Assuming nonzero and finite $N(k,t)$ for all k's at any time, the FZs for $\mathcal{L}(t)$ in Eq. (9) can be determined from $w(n,k)$ for different positive integer n, where

$$w(n,k) := i\frac{\pi(2n+1)}{2\epsilon_k^{\rm f}} + \frac{1}{\epsilon_k^{\rm f}}\tanh^{-1}\left(\hat{d}_k^{\rm i}\cdot\hat{d}_k^{\rm f}\right). \tag{12}$$

Similar to the Hermitian case, the critical times for the DPT are calculated from the imaginary intercept of the curve $w(n,k)$ over the BZ, $k \in (-\pi, \pi]$ on the parametric complex plane [55,62,63]. The momentum for which the imaginary intercept happens is termed critical momentum (k_c^n), and is found from the solution of the equation $\mathrm{Re}[w(n,k_c^n)] = 0$, i.e.,

$$\pi\left(n + \tfrac{1}{2}\right)\mathrm{Im}\left[\epsilon_{k_c^n}^{\rm f}\right] + \mathrm{Re}\left[\left(\epsilon_{k_c^n}^{\rm f}\right)^{*}\tanh^{-1}\left(\hat{d}_{k_c^n}^{\rm i}\cdot\hat{d}_{k_c^n}^{\rm f}\right)\right] = 0. \tag{13}$$

For Hermitian models (i.e., $\mathrm{Im}[\epsilon_k^{\rm f}] = 0$), the above equation can be expressed as $\tanh^{-1}(\hat{d}_{k_c^n}^{\rm i}\cdot\hat{d}_{k_c^n}^{\rm f}) = 0$. Consequently, the FZs emerge symmetrically in the BZ at $\pm k_c^n$. For the quenches by a non-Hermitian $H_{\rm f}$ in the trivial and topological phase in Secs. III A and III C, $\mathrm{Im}[\epsilon_k^{\rm f}] \ll \mathrm{Re}[\epsilon_k^{\rm f}]$ as can be seen in Figs. 2(a) and 2(c). Thus, the FZs emerge in both the positive and negative BZ like the Hermitian case. However, the contribution from $\mathrm{Im}[\epsilon_{k_c}^{\rm f}]$ in Eq. (13) disrupts the above symmetry of FZs for a non-Hermitian $H_{\rm f}$ in comparison for a Hermitian $H_{\rm f}$. Therefore, the FZs occur at different values of k_c^{n+} and k_c^{n-} in the BZ. The corresponding critical time ($t_c^{n\pm}$) when the

DPT occurs is $\mathrm{Im}[w(n, k_c^{n\pm})]$, i.e.,

$$t_c^{n\pm} = \frac{\pi\left(n+\frac{1}{2}\right)\mathrm{Re}\left[\epsilon^{\mathrm{f}}_{k_c^{n\pm}}\right] + \mathrm{Im}\left[\left(\epsilon^{\mathrm{f}}_{k_c^{n\pm}}\right)^* \tanh^{-1}\left(\hat{d}^{\mathrm{i}}_{k_c^{n\pm}} \cdot \hat{d}^{\mathrm{f}}_{k_c^{n\pm}}\right)\right]}{\left|\epsilon^{\mathrm{f}}_{k_c^{n\pm}}\right|^2}. \tag{14}$$

In the Hermitian limit (i.e., $\mathrm{Im}[\epsilon_k^{\mathrm{f}}] = 0$), Eq. (14), $t_c^{n\pm} = \pi(n+\frac{1}{2})/|\epsilon^{\mathrm{f}}_{k_c^{n\pm}}|$, which is degenerate for positive and negative critical momentum and also periodic in time. However, the contribution from the second term in Eq. (14), particularly due to the real part of the band energy, breaks the above degeneracy and periodicity. For H_{f} in the Möbius phase, the real and imaginary parts of ϵ_k^{f} are comparable as shown in Fig. 2(b), and we need to carefully understand the role of $\mathrm{Im}[\epsilon_k^{\mathrm{f}}]$ in Eq. (13). Since $\mathrm{Im}[\epsilon_k^{\mathrm{f}}]$ and $\mathrm{Re}[\epsilon_k^{\mathrm{f}}]$ are, respectively, an odd and even function of k, the relation in Eq. (13) can only be satisfied on one side (either negative or positive) of the BZ when $\mathrm{Im}[\epsilon_k^{\mathrm{f}}]$ and $\mathrm{Re}[\epsilon_k^{\mathrm{f}}]$ are comparable, as we find in Secs. III B and III D.

The nonanalyticity in $I(t)$ indicates the vanishing overlap between evolved and initial states for some $k_c^{n\pm}$ at time $t_c^{n\pm}$, i.e., $\langle\chi^{\mathrm{i},-}_{k_c^{n\pm}}(0)|\psi^{\mathrm{i},-}_{k_c^{n\pm}}(t_c^{n\pm})\rangle = 0$. Such orthogonality between states emerges due to the transition of a particle at momentum $k_c^{n\pm}$ from the filled lower band to the empty upper band at time $t_c^{n\pm}$.

C. Dynamical topological order parameter

Due to translation symmetry within the PBC, the momentum k is a good quantum number for our model, and it remains invariant under quench as we do not change the total length of the chain. The dynamical evolution of each particle is thus independent and separable from others. We can quantify the phase $\phi^G(k,t)$ of such nonadiabatic evolution of a single particle at any time t using the overlap of consecutive instantaneous nonorthogonal states following Pancharatnam's description, which leads to $\phi^G(k,t) = \phi^{\mathrm{LE}}(k,t) - \phi^{\mathrm{dyn}}(k,t)$ [8,64]. Here, $\phi^{\mathrm{LE}}(k,t)$ and $\phi^{\mathrm{dyn}}(k,t)$ denote, respectively, the Loschmidt echo phase and the dynamical phase for the evolution as given by

$$\phi^{\mathrm{LE}}(k,t) = -i\log\frac{\mathcal{G}_k(t)}{|\mathcal{G}_k(t)|}, \tag{15}$$

$$\phi^{\mathrm{dyn}}(k,t) = -i\int_0^t d\tau\,\left\langle\chi_k^{\mathrm{i},-}(\tau)\right|\frac{d}{d\tau}\left|\psi_k^{\mathrm{i},-}(\tau)\right\rangle, \tag{16}$$

$$\left|\psi_k^{\mathrm{i},-}(\tau)\right\rangle = \frac{e^{iH_{\mathrm{f}}\tau}\left|\psi_k^{\mathrm{i},-}(0)\right\rangle}{\sqrt{\left\langle\chi_k^{\mathrm{i},-}(0)\right|e^{-iH_{\mathrm{f}}^\dagger\tau}e^{iH_{\mathrm{f}}\tau}\left|\psi_k^{\mathrm{i},-}(0)\right\rangle}}, \tag{17}$$

$$\left\langle\chi_k^{\mathrm{i},-}(\tau)\right| = \frac{\left\langle\chi_k^{\mathrm{i},-}(0)\right|e^{-iH_{\mathrm{f}}^\dagger\tau}}{\sqrt{\left\langle\chi_k^{\mathrm{i},-}(0)\right|e^{-iH_{\mathrm{f}}^\dagger\tau}e^{iH_{\mathrm{f}}\tau}\left|\psi_k^{\mathrm{i},-}(0)\right\rangle}}. \tag{18}$$

Here, $|\psi_k^{\mathrm{i},-}(\tau)\rangle$ is the instantaneous normalized ket vector at time τ, and the associated bra vector is $\langle\chi_k^{\mathrm{i},-}(\tau)|$. To access the topological change of the aforementioned dynamic process, a dynamical topological order parameter is defined as a time-dependent winding number $[\nu_\pm(t)]$ over the positive or negative momenta of the BZ [6]. It is given by the relation

$$\nu_\pm(t) = -\frac{1}{2\pi}\int_0^{\pm\pi}\frac{\partial\phi^G(k,t)}{\partial k}dk. \tag{19}$$

For a fully Hermitian quench between the initial and final Hermitian SSH Hamiltonian in different topological phases, the chiral symmetry of the SSH chain leads to the quantization of the winding number $\nu_\pm(t)$ and enforces the condition $\phi^G(0, t \neq t_c^n) = \phi^G(\pi, t \neq t_c^n) = 0$ [7]. Consequently, for $k \in [0,\pi)$, the function $\phi^G(t) : [0, 2\pi) \to S^1$ represents a continuous curve on the unit circle. For quenches with a final Hamiltonian of the NSSH model, the above relation for the Pancharatnam phase remains true. We show below in Sec. III that $\nu_\pm(t)$ remains quantized for topology-changing quenches by the NSSH Hamiltonian in the trivial, topological, or Möbius phase.

The existence of dynamical topological order parameter (DTOPs) is generally argued due to the presence of a nontrivial topological change between the initial and final Hamiltonian [7,8,65]. It has been observed that quenches between topologically distinct Hamiltonians with a change in winding number $\Delta\omega$ give at least $2\Delta\omega$ topologically protected DTOPs over the BZ [7]. Therefore, a nonzero DTOP indicates a dynamical topological phase transition induced by quenching between topologically nonequivalent Hamiltonians. In contrast, for quenches between topologically equivalent Hamiltonians, the DTOP is zero, which indicates the sum over the change in the Pancharatnam geometric phases of all momenta, i.e., $\nu_\pm(t)$ is zero. For the NSSH model, while the geometric phase or topological invariant in the trivial or topological phase is defined for individual bands, it is only defined for both bands together in the Möbius phase. This poses a challenge to relate the change in winding number to the number of DTOPs. Here, we implement different quenches by a non-Hermitian Hamiltonian to address these issues regarding the appearance of DTOPs and their counts. A subsequent interpretation of these findings is the main result of our present work.

III. RESULTS

We now present our numerical results of the quench dynamics due to a non-Hermitian SSH final Hamiltonian to an initial state $|\Psi\rangle$ of the Hermitian SSH model, which leads to $\mathcal{L}(t) = \langle\Psi|e^{iH_{\mathrm{f}}t}|\Psi\rangle$. Thus, the initial state of H_{i} can be in the trivial or topological phase, and the parameters of H_{f} can be chosen to be in the trivial, Möbius, or topological phase. Out of these six different possibilities of quench, we focus on the following four nonequivalent topology-changing quenches from initial to final Hamiltonian: (i) topological to trivial, (ii) topological to Möbius, (iii) trivial to topological, and (iv) trivial to Möbius.

A. Topological → trivial

We start by investigating how the features of the Loschmidt echo alter from a fully Hermitian quench for a non-Hermitian H_{f}. So we explore a quench from an initial Hermitian topological phase with parameters $\delta_{\mathrm{i}} = 0.9, \theta_{\mathrm{i}} = 0$ to a non-Hermitian trivial phase of parameters $\delta_{\mathrm{f}} = -0.9$, $\theta_{\mathrm{f}} = 0.4$. Figure 3

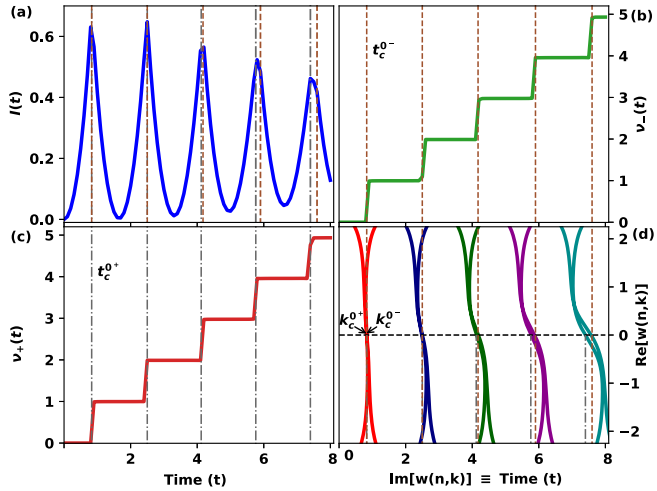

FIG. 3. Return rate $I(t)$ in (a), DTOP over negative momentum $\nu_-(t)$ in (b), and DTOP over positive momentum $\nu_+(t)$ in (c) as a function of time. Fisher zero lines in the complex plane of $w(n,k)$ over the BZ, $k \in (-\pi,\pi]$ (for $n = 0, 1, \ldots, 4$) in (d). Points of intersection of the Fisher zero lines and the dashed black line indicate critical momentum $k_c^{n\pm}$. Dashed brown (dashed-dotted gray) vertical lines through these points correspond to critical times t_c^{n-} (t_c^{n+}). Initial and final Hamiltonian parameters are $\delta_i = 0.9$, $\theta_i = 0$, $\delta_f = -0.9$, $\theta_f = 0.4$.

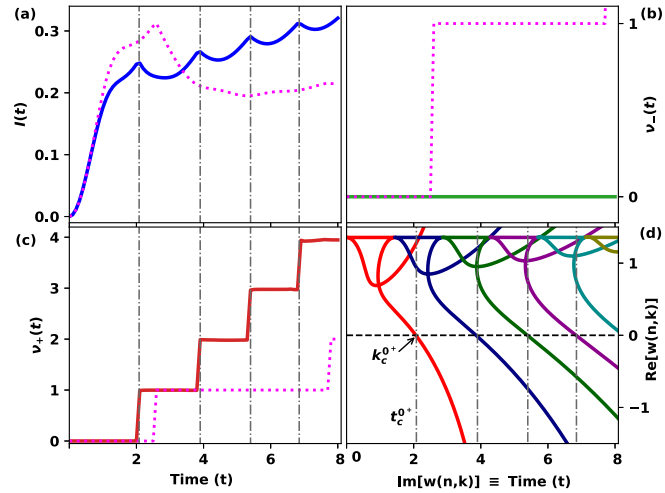

FIG. 4. Return rate $I(t)$ in (a), DTOP over negative momentum $\nu_-(t)$ in (b), and DTOP over positive momentum $\nu_+(t)$ in (c) as a function of time. Fisher zero lines in the complex plane of $w(n,k)$ over the BZ, $k \in (-\pi,\pi]$ (for $n = 0, 1, \ldots, 4$) in (d). Parameters for topological to Möbius quench are $\delta_i = 0.9$, $\theta_i = 0 \Rightarrow \delta_f = -0.1$, $\theta_f = 0.4$. Vertical dashed-dotted gray lines show critical times (t_c^{n+}) corresponding to positive critical momenta (k_c^{n+}). $I(t)$ and DTOPs in the Hermitian limit ($\theta_f = 0$) are depicted by pink dotted lines.

displays the return rate, DTOP, and FZs for such quench dynamics in a chain of $L = 1000$. Despite the non-Hermitian complex energies involved in quench dynamics, the nonanalyticities (sharp cusps) in $I(t)$ in Fig. 3(a) survive, which can be sharp as in the fully Hermitian case [66]. Nevertheless, the periodicity of these peaks is broken for non-Hermitian quenches due to the lifting of degeneracies of the FZs, which are present in the fully Hermitian case. In Fig. 3(d), the FZs for various curves of different n are shown using the cuts by the horizontal dashed line with these curves over the entire BZ, which confirms the presence of these nonanalyticities at critical $k_c^{n\pm}$'s.

The imaginary values of these curves $w(n,k)$ at $k_c^{(n\pm)}$'s in Fig. 3(d) are indicated by the vertical lines, and they represent the critical times $t_c^{n\pm}$ for the DPT. In Figs. 3(b) and 3(c), we show the associated DTOPs, $\nu_\pm(t)$, as a function of time for a quantitative characterization of the DPT. Both the DTOPs depict a discontinuity precisely at the critical times and remain constant between two consecutive nonanalyticities in Figs. 3(b) and 3(c). The quantized sharp jumps in the DTOP have been associated with a dynamical change in the topological character of the evolving state from the initial ground state with particular topological features, and the plateaus between the sharp jumps in the DTOP indicate no change in the topological nature of the evolving state. For quenches in fully Hermitian models, $k_c^{n+} = -k_c^{n-}$ and $t_c^{n+} = t_c^{n-}$. Such degeneracy in $k_c^{n\pm}$ and $t_c^{n\pm}$ is lifted due to a small but nonzero imaginary part of band energies. The maximum imaginary band energy for our particular choice of H_f is $\pm 0.025i$, which is relatively smaller than the real energy of order of ± 2. Thus, the split in $|k_c^{n\pm}|$ and the related periodicity in time is less. The FZs in Fig. 3(d) show these splits over the entire BZ for each n, which explains the jumps in the DTOP calculated for the negative and positive momentum in Figs. 3(b) and 3(c).

B. Topological → Möbius

In this paper, we are mainly interested in studying the quench dynamics by the non-Hermitian H_f in the Möbius phase, which does not have a Hermitian counterpart. We prepare the initial state $|\psi_k^{i,-}(0)\rangle$ in the topological regime of the Hermitian SSH chain (e.g., $\delta_i = 0.9$, $\theta_i = 0$), and quench it by non-Hermitian H_f with parameters $\delta_f = -0.1$, $\theta_f = 0.4$ hosting the Möbius phase. Figure 4(a) shows $I(t)$ with t, which displays peaks indicating nonanalyticities at critical time t_c^{n+}'s. However, the height of these peaks is relatively low compared to the previous case in Fig. 3(a), and $I(t)$ increases overall with time rather than returning closer to zero. The last trend sheds light on the evolving state $|\psi_k^{i,-}(t)\rangle$, which never returns closer to $|\psi_k^{i,-}(0)\rangle$ after such a quench and moves far away from $|\psi_k^{i,-}(0)\rangle$ with progressing time. The breakdown of TRS and the emergence of PHS† give rise to a large and purely imaginary band gap ($0.5i$ for our parameters) at the EPs in the Möbius phase, which leads to a stronger decay of the initial state in the quench process. Interestingly, the FZ degeneracy is completely lifted in this case. Figure 4(d) shows FZs only in the positive momentum range of the BZ, and there is no FZ for negative momentum. As discussed earlier in Sec. II B, this behavior stems from the even and odd k-dependence of the real and imaginary part of $E_p(k)$, the values of which are mostly comparable in the Möbius phase between the EPs [12,29]. We present the DTOPs of Eq. (19) in Figs. 4(b) and 4(c), which show the presence (absence) of a sharp jump in $\nu_+(t)$ [$\nu_-(t)$] with time in the presence

(absence) of FZs in the positive (negative) momentum BZ. While the topological invariant and winding number are only defined for both the complex bands together in the Möbius phase, we can draw an analogy here for the non-Hermitian quenches to the observation for Hermitian quenches [7] by relating the $2\Delta\omega$ number (which is 1) of DTOP in the entire BZ for a change in winding number from the topological to the Möbius phase as $\Delta\omega = 0.5$. Thus, we assume the winding number for each band in the Möbius phase is half [see Fig. 2(e)]. Similar features of $I(t)$ are also observed when the initial state $|\psi_k^{i,-}(0)\rangle$ is switched to $|\psi_k^{i,+}(0)\rangle$ as a filled upper band. However, the FZs instead appear only in the negative momentum of the BZ.

In Figs. 4(a)–4(c), we also include the plots of $I(t)$ and DTOPs by pink dotted lines for the fully Hermitian quench for such a parameter regime by setting $\theta_f = 0$. These plots show a topological to trivial quench dynamics for a fully Hermitian system because the non-Hermitian Möbius phase lies at the boundary of the Hermitian trivial phase for our parameters. The critical times for the Hermitian quench is longer than the related non-Hermitian quench due to a lower energy gap. Figures 4(b) and 4(c) also display the presence of DTOPs in both the positive and negative momentum of the BZ for a Hermitian quench. Thus, the non-Hermiticity induces a directional DTOP, which depends on the choice of the initial ground state. Our results for DTOP in Fig. 4 also confirm the nontrivial topological character of the Möbius phase.

C. Trivial → topological

Next, we consider a quench from $|\psi_k^{i,-}(0)\rangle$ of Hermitian H_i in the trivial phase (e.g., $\delta_i = -0.9,\ \theta_i = 0$) by non-Hermitian H_f in the topological phase for $\delta_f = 0.9,\ \theta_f = 0.4$. Similar to those in Sec. III A, $I(t)$ again features an excellent return close to the initial state at shorter times in Fig. 5(a). Nevertheless, the sharp cusps in $I(t)$ split into two more noticeably than those in Fig. 3(a). The splittings indicate the breaking of degeneracies in the magnitude of critical positive and negative momentum as shown in Fig. 5(d), and discussed after Eq. (13). The higher splittings in Fig. 5(a) in comparison to Fig. 3(a) are due to higher values of contributing real energies (max. 2.5) of the complex bands [Eq. (14)]. We observe that $\theta \to 0$ and $|\delta| \to 1$ are favorable conditions to avoid such splittings. Since the change in winding number between H_i and H_f is 1, the FZs in Eq. (12) sweep through the imaginary axis two times as k goes through the BZ in Fig. 5(d). Further, the Pancharatnam geometric phase $[\phi_G(k,t)]$ shows a clear jump of 2π over the negative and positive momentum range of the BZ in Fig. 1(b), which indicates the appearance of quantized DTOPs in the negative and positive momentum range in Figs. 5(b) and 5(c) showing a good alignment with the corresponding critical times $t_c^{n\pm}$ and FZs in Fig. 5(d). The width of the split in the nonanalyticities of $I(t)$ can be controlled by the system parameters $\theta,\ \delta$.

D. Trivial → Möbius

Since the entire Möbius phase for our choice of parameters appears in the trivial phase region of the corresponding Hermitian model, a nontrivial quench dynamics from

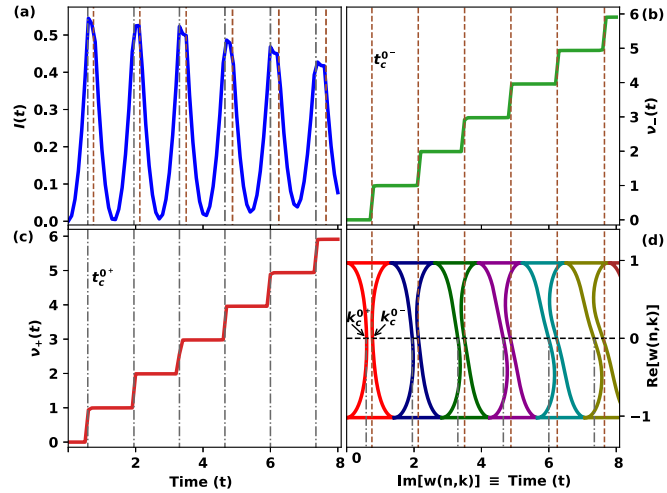

FIG. 5. Return rate $I(t)$ in (a), DTOP over negative momentum $\nu_-(t)$ in (b), and DTOP over positive momentum $\nu_+(t)$ in (c) as a function of time. Fisher zero lines in the complex plane of $w(n,k)$ over the BZ, $k \in (-\pi, \pi]$ (for $n = 0, 1, \ldots, 4$) in (d). Parameters for trivial to topological quench are $\delta_i = -0.9,\ \theta_i = 0 \Rightarrow \delta_f = 0.9,\ \theta_f = 0.4$. DTOPs in the positive and negative momentum of the BZ ($\pm$) are aligned with the critical times $t_c^{n\pm}$ (vertical lines) and the corresponding critical momenta $k_c^{n\pm}$.

$|\psi_k^{i,-}(0)\rangle$ of Hermitian H_i in the trivial phase (e.g., $\delta_i = -0.9,\ \theta_i = 0$) by non-Hermitian H_f in the Möbius phase boundary for $\delta_f = -0.1,\ \theta_f = 0.4$ is very significant for establishing special topological features of the Möbius phase. We remind the reader that there is neither any nonanalyticity in $I(t)$ nor a finite DTOP in the corresponding fully Hermitian quench as displayed in Fig. 6 by the pink dotted lines. The

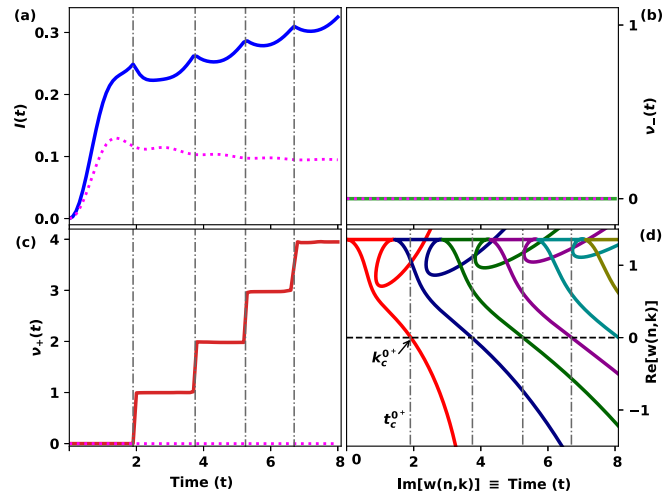

FIG. 6. Return rate $I(t)$ in (a), DTOP over negative momentum $\nu_-(t)$ in (b), and DTOP over positive momentum $\nu_+(t)$ in (c) as a function of time. Fisher zero lines in the complex plane of $w(n,k)$ over the BZ, $k \in (-\pi, \pi]$ (for $n = 0, 1, \ldots, 4$) in (d). Parameters for topological to Möbius quench are $\delta_i = -0.9,\ \theta_i = 0 \Rightarrow \delta_f = -0.1,\ \theta_f = 0.4$. Vertical lines indicate critical times t_c^{n+} for critical momenta k_c^{n+} in the BZ ($k \in [0, \pi]$). $I(t)$ and DTOPs in the Hermitian limit ($\theta_f = 0$) are depicted by pink dotted lines.

above non-Hermitian quench follows similar trends of the quench in Sec. III B from the topological to the Möbius phase. For example, $I(t)$ in Fig. 6(a) shows cusps with small heights, and it moves away from the initial state with longer timescales similar to Fig. 4(a). The position of these nonanalyticities around the cusps can be determined by the imaginary intercept of the FZs [in Eq. (12)] for different n imprinted in Fig. 6(d). Resembling the topological-Möbius quench, the Fisher zero lines cut imaginary axis only in the momentum $k \in [0, \pi]$ in Fig. 6(d). The corresponding DTOPs in this range are presented in Fig. 6(c), and there is no DTOP in Fig. 6(b) for the negative momentum of the BZ due to the absence of FZs.

These DTOPs are reminiscent of $\phi_G(k, t)$ in Fig. 1(a) showing 2π jump only at one side of the BZ. The other DTOP appears for negative momentum for a quench from an initial state in the upper energy band due to the symmetry constraints on the complex energy bands' real and imaginary parts as discussed in Sec. III B. Comparing the plots of $I(t)$ and DTOP between the Hermitian and non-Hermitian quenches in Fig. 6, we argue that non-Hermiticity gives rise to the Möbius phase with exciting dynamical topological features in the nonequilibrium setups due to spontaneous breaking of TRS and the emergence of PHS† [12,29]. It should be further noted that there is no significant difference obtained in $I(t)$ and DTOPs between the topological-Möbius quench and the trivial-Möbius quench. The last is due to the PBC employed in these studies, which reminds us of the fully Hermitian case where a symmetric trivial-topological and a topological-trivial quench are not differentiable for PBC [67].

IV. SUMMARY AND OUTLOOK

In this work, we have shown new dynamical properties of the recently discovered composite Möbius phase of sublattice symmetric non-Hermitian models to confirm the unique topological character of the phase. One of the main findings is the appearance of the DTOP in quench dynamics by the non-Hermitian SSH Hamiltonian in the Möbius phase indicating topological differences of the Möbius phase from the other two phases (namely, trivial and topological phases) of the non-Hermitian SSH model. Moreover, the DTOP appears only at one side of the BZ for any particular choice of the initial state, which is a dynamical signature of different symmetry constraints on the real and imaginary parts of the complex bands in the Möbius phase. The above features of DTOPs are significantly different for the other two non-Hermitian topological phases (trivial and nontrivial) with Hermitian counterparts, where the presence of a large complex band gap ensures that two DTOPs in the BZ for quenches between these distinct topological phases differed by one winding number. Since the appearance of DTOPs on one side of the BZ depends critically on the comparability of the real and imaginary parts of the band energy, the boundaries for the emergence of one-sided versus both-sided DTOPs are not sharp but rather depend on the parameters of quench for the final Hamiltonians. The experiments on the dynamical studies of these new non-Hermitian topological phases could lead to a deeper connection between these topological states' robustness [68].

We have employed the time evolution of biorthogonal states given in Eqs. (17) and (18) following the Schrödinger equation and by normalizing it at each instant. This is an approximate scheme for non-Hermitian systems [69,70]. Nevertheless, other schemes, such as the metric method [71,72], can be tested for such dynamical studies. We believe that the position of nonanalyticities of $I(t)$ at the FZs would not change for a different scheme. Further, while the conventional quantum phase transitions are accompanied by an emergence of a local order parameter due to spontaneous symmetry breaking in one phase, no such local order parameter or spontaneous symmetry breaking is associated with a topological phase transition in equilibrium [45]. The topological phase transitions in Hermitian systems are instead classified by topological invariants. However, the topological changes in non-Hermitian systems are also in some cases accompanied by spontaneous symmetry breaking, although without emergence of a local order parameter. The signatures of dynamical quantum phase transitions, e.g., the nonanalyticities of $I(t)$, seem similar to those for dynamical topological phase transitions. Thus, both these dynamical phase transitions have been unified in out-of-equilibrium systems.

In our earlier work [12], we have extended the research on sublattice symmetric non-Hermitian SSH models by going beyond bipartite models to tripartite and quadripartite models with three and four sublattice sites per unit cell, respectively. Such an extension generates various non-Hermitian topological insulating and metallic composite phases with nontrivial topology like the Penrose triangle. It would be exciting to explore quench dynamics by a final Hamiltonian in such composite phases to understand the dynamical properties of such topological phases. While there are many experimental realizations of $\mathcal{PT}$ symmetric non-Hermitian models in engineered photonic, cold atomic, phononic, and electrical systems, the nonreciprocal hopping for sublattice symmetric non-Hermitian models has only recently been realized [13,73–76]. Thus, these non-Hermitian models can be explored to experimentally probe $I(t)$ and DTOPs following the implementation in the Hermitian settings [55–57,60,61,65,77].

ACKNOWLEDGMENT

We thank Kiran Estake for many useful discussions.

APPENDIX: CONTRIBUTION OF BOUNDARY MODES TO RETURN RATE

In this Appendix, we present the boundary modes' contribution to the return rate of a many-body initial state after a quench. It is now well established that the conventional bulk-boundary correspondence of Hermitian topological systems fails in non-Hermitian models [16,36,37,78–80]. In simpler terms, the bulk energy spectrum of such models for PBC does not match with that for an open boundary. Nevertheless, it is possible to reinstate the bulk-boundary correspondence by replacing the open boundary with some particular boundary asymptotically matching the open boundary [11,81–83]. Here, we are interested in the boundary contribution to the return rate of an initial state after a quench by a non-Hermitian Hamiltonian in Eq. (1) with a boundary parameter, i.e., $\eta = 1/L$ [11] (loose connection).

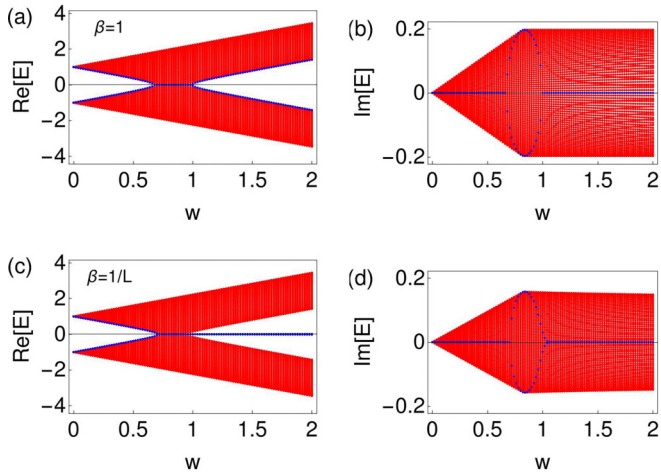

FIG. 7. The real (a,c) and imaginary (b,d) energy spectrum of the NSSH model as a function of intercell hopping parameter w for periodic $\eta = 1$ (a,b) and special $\eta = 1/L$ (c,d) boundary. The parameters are $v_l = v_r = 1$, $w_l = we^{\theta}$, $w_r = w$, $\theta = 0.4$, $L = 100$.

To study such a boundary contribution to the return rate, it is essential to understand first the energy spectrum and eigenstates of the non-Hermitian system under these boundary conditions. The complex energy spectrum of the NSSH model with the choice of parameters $v_l = v_r = v = 1$, $w_r = w$, $w_l = we^{\theta}$ is shown in Fig. 7 for periodic ($\eta = 1$) and special ($\eta = 1/L$) boundaries. For PBC, the blue lines in Fig. 7 represent the energies at the band edges within the band-gap region. They can also denote the edge modes near zero energies for special boundaries. The energies of these blue lines are real and nonzero in the trivial phase ($w < ve^{-\theta}$). In comparison, these energies are purely imaginary in the Möbius phase ($ve^{-\theta} < w < v$), and they are real and close to zero in the topological phase ($w > v$).

In Fig. 8, we present the corresponding eigenstates related to the energies denoted by blue lines in three different phases for the special boundary. The eigenstate in Fig. 8(a) in the

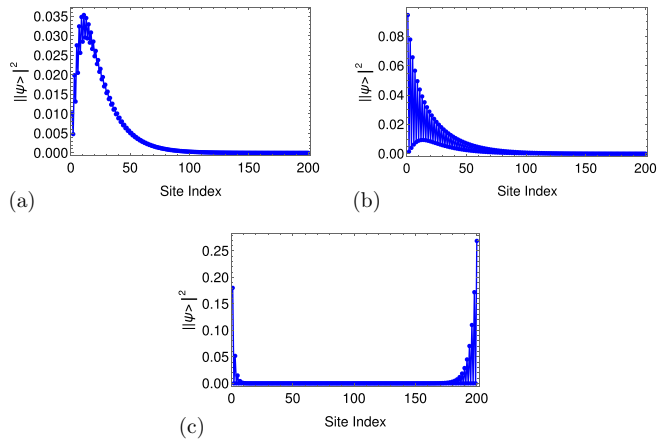

FIG. 8. The spatial profile of right eigenvectors ($||\psi\rangle|^2$) corresponding to the energies (a) 0.69, (b) $0.124i$, and (c) 0.0087 for $v_l = v_r = 1$, $w_r = w$, $w_l = we^{\theta}$, $\theta = 0.4$, $L = 100$, $\eta = 1/L$ and (a) $w = 0.25$, (b) $w = 0.75$, (c) $w = 1.25$.

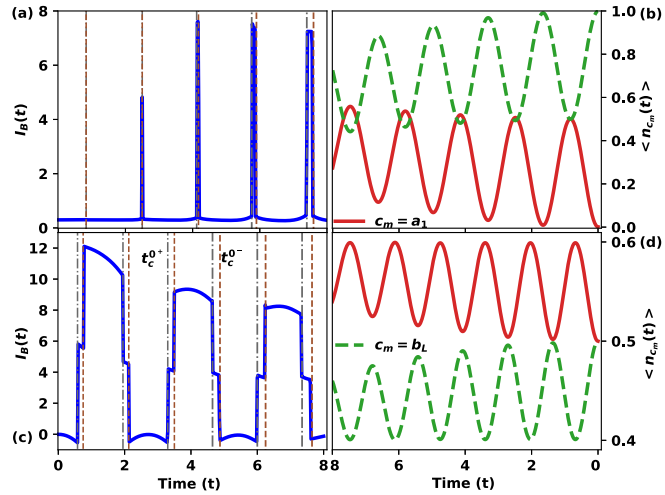

FIG. 9. The boundary contribution to return rate (I_B) in (a,c) and the dynamics of edge occupancy (n_{a_1,b_L}) in (b,d) as a function of time for a quench from a topological to a trivial phase ($\delta_i = -\delta_f = 0.9$, $\theta_i = 0$, $\theta_f = 0.4$) in (a,b), and a trivial to a topological phase ($\delta_i = -\delta_f = -0.9$, $\theta_i = 0$, $\theta_f = 0.4$) in (c,d) for a chain of $L = 500$.

trivial phase is localized towards the left, which indicates the non-Hermitian skin effect [47,49,83]. The eigenstate in Fig. 8(c) is predominantly localized near the edges similar to a Hermitian SSH edge state, and exponentially falls away from the left and right edges with respective localization length, $\xi_L = 1/\log(we^{\theta}/v)$ and $\xi_R = 1/\log(w/v)$. In Fig. 8(b), the eigenstate in the Möbius phase with purely imaginary energy [11] also displays the non-Hermitian skin effect, characterized by a slower exponential fall indicating a longer localization length.

The return rates for Hermitian models for different boundary conditions [67] can be related to each other for a large system size L as

$$I_o(t) \sim I(t) + \frac{I_B(t)}{L}, \tag{A1}$$

where $I(t)$ and $I_o(t)$ denote the return rate, respectively, for periodic ($\eta = 1$) and open ($\eta = 0$) boundaries of the system. Here, I_B represents the boundary contribution to the return rate, which infers about the topologically protected edge modes. Next, we study I_B for different quenches in the main paper. Since the final Hamiltonian is non-Hermitian in our study, we impose special ($\eta_f = 1/L, \theta_f = 0.4$) and periodic ($\eta_f = 1, \theta_f = 0.4$) boundaries for the final Hamiltonian when the corresponding initial Hamiltonian is under an open and a periodic boundary, respectively. It helps to find $I_B(t)$ in Figs. 9 and 10. We further try to relate $I_B(t)$ with the dynamics of both edge occupancy, denoted by $n_{c_m}(t) = \langle\psi(t)|c_m^{\dagger}c_m|\psi(t)\rangle$, where $c_m = a_1, b_L$. We can also explore $I_B(t)$ with a special boundary for the initial and final Hamiltonian, and the results remain qualitatively the same for $I_B(t)$ as in Figs. 9 and 10.

The main features of $I(t)$, such as the appearance of nonanalyticities across a topology-changing quench, are also captured by $I_o(t)$. In Figs. 9(a) and 9(c), we show that I_B for quenches by the NSSH Hamiltonian from a topological to a trivial phase and vice versa resembles those in fully Hermitian counterparts [67], respectively. This is due to the topological

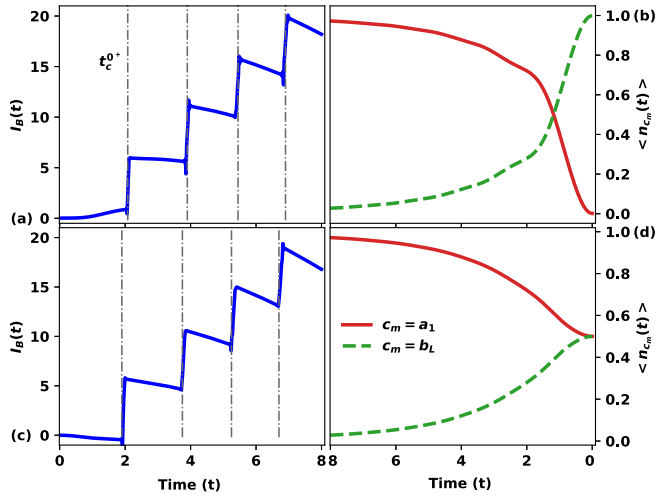

FIG. 10. The boundary contribution to the return rate (I_B) in (a,c) and the dynamics of edge occupancy (n_{a_1,b_L}) in (b,d) as a function of time for a quench from a topological ($\delta_i = 0.9$) to a Möbius phase in (a,b) and a trivial ($\delta_i = -0.9$) to a Möbius phase in (c,d) for a chain of $L = 500$. The other parameters are $\delta_f = -0.1$, $\theta_i = 0$, $\theta_f = 0.4$.

edge modes in these systems, as shown in Fig. 8(c). The magnitude of I_B depends on the topology of the final NSSH Hamiltonian, and the jumps in I_B indicate the nonanalyticity of the return rate [67]. Notably, in the quench from a topological to a trivial phase in the non-Hermitian systems, the boundary contribution in the return rate reveals a more distinct signature of analyticities compared to the Hermitian case.

In Figs. 10(a) and 10(c), we show I_B for quenches from a topological or a trivial to a Möbius phase, respectively. Interestingly, I_B in Figs. 10(a) and 10(c) for these quenches show contrasting features like the DTOPs in comparison to other quenches in Fig. 9. I_B depicts nonanalyticities only at t_c^{0+}'s corresponding to k_c^{0+}'s as in Figs. 4 and 6. Further, the dynamics of edge occupancies in Figs. 10(b) and 10(d) show characteristic differences from those in Figs. 9(b) and 9(d), which are probably due to the purely imaginary energies and the non-Hermitian skin-effect-like features of the edge modes in the Möbius phase. The non-Hermitian skin effect is also evident in the occupancy dynamics after a quench, where regardless of the initial state, the occupancy of the left edge (n_{a_1}) reaches 1, and that of the right edge (n_{b_L}) goes to 0 after some time, as shown in Figs. 10(b) and 10(d).

[1] D. J. Thouless, *Topological Quantum Numbers in Nonrelativistic Physics* (World Scientific, Singapore, 1998).

[2] D. J. Thouless, M. Kohmoto, M. P. Nightingale, and M. den Nijs, Quantized Hall conductance in a two-dimensional periodic potential, Phys. Rev. Lett. **49**, 405 (1982).

[3] D. J. Thouless, Quantization of particle transport, Phys. Rev. B **27**, 6083 (1983).

[4] R. D. King-Smith and D. Vanderbilt, Theory of polarization of crystalline solids, Phys. Rev. B **47**, 1651 (1993).

[5] A. Y. Kitaev, Unpaired Majorana fermions in quantum wires, Phys. Usp. **44**, 131 (2001).

[6] J. C. Budich and M. Heyl, Dynamical topological order parameters far from equilibrium, Phys. Rev. B **93**, 085416 (2016).

[7] S. Vajna and B. Dóra, Topological classification of dynamical phase transitions, Phys. Rev. B **91**, 155127 (2015).

[8] C. B. Mendl and J. C. Budich, Stability of dynamical quantum phase transitions in quenched topological insulators: From multiband to disordered systems, Phys. Rev. B **100**, 224307 (2019).

[9] D. Roy, N. Bondyopadhaya, and S. Tewari, Topologically trivial zero-bias conductance peak in semiconductor Majorana wires from boundary effects, Phys. Rev. B **88**, 020502(R) (2013).

[10] N. Bondyopadhaya and D. Roy, Dynamics of hybrid junctions of Majorana wires, Phys. Rev. B **99**, 214514 (2019).

[11] V. M. Vyas and D. Roy, Topological aspects of periodically driven non-Hermitian Su-Schrieffer-Heeger model, Phys. Rev. B **103**, 075441 (2021).

[12] R. Nehra and D. Roy, Topology of multipartite non-Hermitian one-dimensional systems, Phys. Rev. B **105**, 195407 (2022).

[13] H. Zhang, T. Chen, L. Li, C. H. Lee, and X. Zhang, Electrical circuit realization of topological switching for the non-Hermitian skin effect, Phys. Rev. B **107**, 085426 (2023).

[14] L. Jin, Topological phases and edge states in a non-Hermitian trimerized optical lattice, Phys. Rev. A **96**, 032103 (2017).

[15] S. Longhi, D. Gatti, and G. Della Valle, Non-Hermitian transparency and one-way transport in low-dimensional lattices by an imaginary gauge field, Phys. Rev. B **92**, 094204 (2015).

[16] A. Ghatak, M. Brandenbourger, J. van Wezel, and C. Coulais, Observation of non-Hermitian topology and its bulk–edge correspondence in an active mechanical metamaterial, Proc. Natl. Acad. Sci. USA **117**, 29561 (2020).

[17] J. Jiang, B. Yan, Y. Peng, J. Xie, A. Shi, and J. Liu, Multiband topological states in non-Hermitian photonic crystals, Opt. Lett. **47**, 437 (2022).

[18] M. Berry, Physics of non-Hermitian degeneracies, Czech. J. Phys. **54**, 1039 (2004).

[19] H. Cartarius, J. Main, and G. Wunner, Exceptional points in the spectra of atoms in external fields, Phys. Rev. A **79**, 053408 (2009).

[20] H. Xu, D. Mason, L. Jiang, and J. G. E. Harris, Topological energy transfer in an optomechanical system with exceptional points, Nature (London) **537**, 80 (2016).

[21] N. Hatano and D. R. Nelson, Localization transitions in non-Hermitian quantum mechanics, Phys. Rev. Lett. **77**, 570 (1996).

[22] R. Okugawa, R. Takahashi, and K. Yokomizo, Non-Hermitian band topology with generalized inversion symmetry, Phys. Rev. B **103**, 205205 (2021).

[23] K. Wang, A. Dutt, C. C. Wojcik, and S. Fan, Topological complex-energy braiding of non-Hermitian bands, Nature (London) **598**, 59 (2021).

[24] H. Hu and E. Zhao, Knots and non-Hermitian Bloch bands, Phys. Rev. Lett. **126**, 010401 (2021).

[25] D. S. Borgnia, A. J. Kruchkov, and R.-J. Slager, Non-Hermitian boundary modes and topology, Phys. Rev. Lett. **124**, 056802 (2020).

[26] W. D. Heiss, The physics of exceptional points, J. Phys. A **45**, 444016 (2012).

[27] W. D. Heiss, Chirality of wave functions for three coalescing levels, J. Phys. A **41**, 244010 (2008).

[28] K. Kawabata, K. Shiozaki, M. Ueda, and M. Sato, Symmetry and topology in non-Hermitian physics, Phys. Rev. X **9**, 041015 (2019).

[29] K. Kawabata, S. Higashikawa, Z. Gong, Y. Ashida, and M. Ueda, Topological unification of time-reversal and particle-hole symmetries in non-Hermitian physics, Nat. Commun. **10**, 297 (2019).

[30] K. Kawabata, Y. Ashida, H. Katsura, and M. Ueda, Parity-time-symmetric topological superconductor, Phys. Rev. B **98**, 085116 (2018).

[31] K. Ding, C. Fang, and G. Ma, Non-Hermitian topology and exceptional-point geometries, Nat. Rev. Phys. **4**, 745 (2022).

[32] S. Lieu, Topological phases in the non-Hermitian Su-Schrieffer-Heeger model, Phys. Rev. B **97**, 045106 (2018).

[33] C. Yin, H. Jiang, L. Li, R. Lü, and S. Chen, Geometrical meaning of winding number and its characterization of topological phases in one-dimensional chiral non-Hermitian systems, Phys. Rev. A **97**, 052115 (2018).

[34] H. Shen, B. Zhen, and L. Fu, Topological band theory for non-Hermitian Hamiltonians, Phys. Rev. Lett. **120**, 146402 (2018).

[35] T. E. Lee, Anomalous edge state in a Non-Hermitian lattice, Phys. Rev. Lett. **116**, 133903 (2016).

[36] F. K. Kunst, E. Edvardsson, J. C. Budich, and E. J. Bergholtz, Biorthogonal bulk-boundary correspondence in Non-Hermitian systems, Phys. Rev. Lett. **121**, 026808 (2018).

[37] S. Yao and Z. Wang, Edge states and topological invariants of Non-Hermitian systems, Phys. Rev. Lett. **121**, 086803 (2018).

[38] L. Zhou, Q.-H. Wang, H. Wang, and J. Gong, Dynamical quantum phase transitions in non-Hermitian lattices, Phys. Rev. A **98**, 022129 (2018).

[39] X. Qiu, T.-S. Deng, Y. Hu, P. Xue, and W. Yi, Fixed points and dynamic topological phenomena in a parity-time-symmetric quantum quench, iScience **20**, 392 (2019).

[40] J.-C. Tang, S.-P. Kou, and G. Sun, Dynamical scaling of Loschmidt echo in non-Hermitian systems, Europhys. Lett. **137**, 40001 (2022).

[41] S. Longhi, Loschmidt echo and fidelity decay near an exceptional point, Ann. Phys. (Berl.) **531**, 1900054 (2019).

[42] L. Zhou and Q. Du, Non-Hermitian topological phases and dynamical quantum phase transitions: a generic connection, New J. Phys. **23**, 063041 (2021).

[43] D. Mondal and T. Nag, Anomaly in the dynamical quantum phase transition in a non-Hermitian system with extended gapless phases, Phys. Rev. B **106**, 054308 (2022).

[44] W. P. Su, J. R. Schrieffer, and A. J. Heeger, Soliton excitations in polyacetylene, Phys. Rev. B **22**, 2099 (1980).

[45] J. K. Asbóth, L. Oroszlány, and A. Pályi, *A Short Course on Topological Insulators: Band-structure Topology and Edge States in One and Two Dimensions* (Springer, Heidelberg, Germany, 2016).

[46] N. Okuma, K. Kawabata, K. Shiozaki, and M. Sato, Topological origin of non-Hermitian skin effects, Phys. Rev. Lett. **124**, 086801 (2020).

[47] C. Yuce, Non-Hermitian anomalous skin effect, Phys. Lett. A **384**, 126094 (2020).

[48] X. Zhang, G. Li, Y. Liu, T. Tai, R. Thomale, and C. H. Lee, Tidal surface states as fingerprints of non-Hermitian nodal knot metals, Commun. Phys. **4**, 47 (2021).

[49] L. Li, C. H. Lee, S. Mu, and J. Gong, Critical non-Hermitian skin effect, Nat. Commun. **11**, 5491 (2020).

[50] J.-Q. Li, J.-J. Li, L. Qi, Z.-X. Zhang, J. Cao, W.-X. Cui, S. Zhang, and H.-F. Wang, Symmetry and topology of the topological counterparts in non-Hermitian systems, Ann. Phys. (Berl.) **535**, 2300133 (2023).

[51] S.-D. Liang and G.-Y. Huang, Topological invariance and global Berry phase in non-Hermitian systems, Phys. Rev. A **87**, 012118 (2013).

[52] H. C. Wu, L. Jin, and Z. Song, Topology of anti-parity-time-symmetric non-Hermitian Su-Schrieffer-Heeger model, Phys. Rev. B **103**, 235110 (2021).

[53] A. Goussev, R. A. Jalabert, H. M. Pastawski, and D. A. Wisniacki, Loschmidt echo, Scholarpedia **7**, 11687 (2012).

[54] M. Sadrzadeh, R. Jafari, and A. Langari, Dynamical topological quantum phase transitions at criticality, Phys. Rev. B **103**, 144305 (2021).

[55] M. Heyl, A. Polkovnikov, and S. Kehrein, Dynamical quantum phase transitions in the transverse-field Ising model, Phys. Rev. Lett. **110**, 135704 (2013).

[56] T. A. Elsayed and B. V. Fine, Sensitivity to small perturbations in systems of large quantum spins, Phys. Scr. **T165**, 014011 (2015).

[57] P. R. Levstein, G. Usaj, and H. M. Pastawski, Attenuation of polarization echoes in nuclear magnetic resonance: A study of the emergence of dynamical irreversibility in many-body quantum systems, J. Chem. Phys. **108**, 2718 (1998).

[58] T. Gorin, T. Prosen, T. H. Seligman, and M. Znidaric, Dynamics of Loschmidt echoes and fidelity decay, Phys. Rep. **435**, 33 (2006).

[59] V. K. Vimal, H. Wanare, and V. Subrahmanyam, Loschmidt echo and momentum distribution in a Kitaev spin chain, Phys. Rev. A **106**, 032221 (2022).

[60] R. Jafari and H. Johannesson, Loschmidt echo revivals: Critical and noncritical, Phys. Rev. Lett. **118**, 015701 (2017).

[61] G. Torre, V. Marić, D. Kuić, F. Franchini, and S. M. Giampaolo, Odd thermodynamic limit for the Loschmidt echo, Phys. Rev. B **105**, 184424 (2022).

[62] S. Peotta, F. Brange, A. Deger, T. Ojanen, and C. Flindt, Determination of dynamical quantum phase transitions in strongly correlated many-body systems using Loschmidt cumulants, Phys. Rev. X **11**, 041018 (2021).

[63] R. Jafari, Dynamical quantum phase transition and quasi particle excitation, Sci. Rep. **9**, 2871 (2019).

[64] S. Pancharatnam, Generalized theory of interference and its applications, Proc. Ind. Acad. Sci. **44**, 398 (1956).

[65] M. Heyl, Dynamical quantum phase transitions: A review, Rep. Prog. Phys. **81**, 054001 (2018).

[66] J. Sirker, M. Maiti, N. P. Konstantinidis, and N. Sedlmayr, Boundary fidelity and entanglement in the symmetry protected topological phase of the SSH model, J. Stat. Mech. (2014) P10032.

[67] N. Sedlmayr, P. Jaeger, M. Maiti, and J. Sirker, Bulk-boundary correspondence for dynamical phase transitions in one-dimensional topological insulators and superconductors, Phys. Rev. B **97**, 064304 (2018).

[68] H. Zhao, X. Qiao, T. Wu, B. Midya, S. Longhi, and L. Feng, Non-Hermitian topological light steering, Science **365**, 1163 (2019).

[69] T. Helbig, T. Hofmann, S. Imhof, M. Abdelghany, T. Kiessling, L. Molenkamp, C. Lee, A. Szameit, M. Greiter, and R. Thomale, Generalized bulk-boundary correspondence in non-Hermitian topolectrical circuits, Nat. Phys. **16**, 747 (2020).

[70] Q. Liang, D. Xie, Z. Dong, H. Li, H. Li, B. Gadway, W. Yi, and B. Yan, Dynamic signatures of non-Hermitian skin effect and topology in ultracold atoms, Phys. Rev. Lett. **129**, 070401 (2022).

[71] A. Mostafazadeh, Energy observable for a quantum system with a dynamical Hilbert space and a global geometric extension of quantum theory, Phys. Rev. D **98**, 046022 (2018).

[72] A. Mostafazadeh, Time-dependent pseudo-Hermitian Hamiltonians and a hidden geometric aspect of quantum mechanics, Entropy **22**, 471 (2020).

[73] B. Liu, Y. Li, B. Yang, X. Shen, Y. Yang, Z. H. Hang, and M. Ezawa, Experimental observation of non-Hermitian higher-order skin interface states in topological electric circuits, Phys. Rev. Res. **5**, 043034 (2023).

[74] L. Xiao, X. Zhan, Z. Bian, K. Wang, X. Zhang, X. Wang, J. Li, K. Mochizuki, D. Kim, N. Kawakami *et al.*, Observation of topological edge states in parity–time-symmetric quantum walks, Nat. Phys. **13**, 1117 (2017).

[75] J. Li, A. K. Harter, J. Liu, L. de Melo, Y. N. Joglekar, and L. Luo, Observation of parity-time symmetry breaking transitions in a dissipative Floquet system of ultracold atoms, Nat. Commun. **10**, 855 (2019).

[76] K. Wang, X. Qiu, L. Xiao, X. Zhan, Z. Bian, B. C. Sanders, W. Yi, and P. Xue, Observation of emergent momentum–time skyrmions in parity–time-symmetric non-unitary quench dynamics, Nat. Commun. **10**, 2293 (2019).

[77] K. Wrześniewski, I. Weymann, N. Sedlmayr, and T. Domański, Dynamical quantum phase transitions in a mesoscopic superconducting system, Phys. Rev. B **105**, 094514 (2022).

[78] Z. Gong, Y. Ashida, K. Kawabata, K. Takasan, S. Higashikawa, and M. Ueda, Topological phases of non-Hermitian systems, Phys. Rev. X **8**, 031079 (2018).

[79] E. J. Bergholtz, J. C. Budich, and F. K. Kunst, Exceptional topology of non-Hermitian systems, Rev. Mod. Phys. **93**, 015005 (2021).

[80] Z.-Q. Zhang, H. Liu, H. Liu, H. Jiang, and X. Xie, Bulk-boundary correspondence in disordered non-Hermitian systems, Sci. Bull. **68**, 157 (2023).

[81] C.-X. Guo, C.-H. Liu, X.-M. Zhao, Y. Liu, and S. Chen, Exact solution of non-hermitian systems with generalized boundary conditions: Size-dependent boundary effect and fragility of the skin effect, Phys. Rev. Lett. **127**, 116801 (2021).

[82] R. Koch and J. C. Budich, Bulk-boundary correspondence in non-Hermitian systems: Stability analysis for generalized boundary conditions, Eur. Phys. J. D **74**, 70 (2020).

[83] E. Edvardsson and E. Ardonne, Sensitivity of non-Hermitian systems, Phys. Rev. B **106**, 115107 (2022).